Improvement of workstation in manufacturing industry for manual handling worker

Z. Abdullah, N.A. Samsuddin, A.A. Stephen*, R.H. Hambali, H. Arep, S. Akmal,
Faculty of Manufacturing Engineering, Universiti Teknikal Malaysia Melaka,
Hang Tuah Jaya, 76100 Durian Tunggal, Melaka, Malaysia

*Corresponding email: amirahafina26@gmail.com

Keywords: muscle fatigue; working posture; ergonomic workstation

ABSTRACT – Manual jobs can make the time-to-fatigue for the workers in industries become shorter especially when they work in awkward posture. Due to awkward working posture, the workers may be exposed to various ergonomics risk factors. Example such as the table's height is fixed, but the heights of the operators are different to each operator. This condition can contribute to low back pain and fatigue to the operator. Thus, the design improvement for the workstation table have been suggested in this project by using the questionnaire, CATIA V5 software, QFD analysis and RULA analysis to analyze and improvise the operator's conditions.

1. INTRODUCTION

Fatigue is a reaction of continuous tiredness or weakness and can be physical, mental or both. According to Williamson et al. [1], the fatigue associated with tiredness and reduced alertness is different from physical fatigue or weariness that is caused by long and/or hard physical work. There are many accidents in the manufacturing industries which are the result of fatigue. Those whose feel fatigued are poor at realising their own level of impairment. The worst case was workers can sleep in the middle of a task, which can have serious consequences. Fatigue, psychosocial workload and insufficient sleep have been recognized as major consequences of this increased work intensity amongst working populations [2].

The growth of muscle fatigue is typically due to rejection in the power capacity of muscle, which means that contractions sustained after the beginning of muscle fatigue. The consequences of fatigue can be categorized as either short-term risk, typically related to poor safety outcomes, and/or long-term risks related to reduced physical and/or psychological health [3]. Differential responses to various types of work exposures can result in highly variable fatigue outcomes [2]. The common example for the disorder is low back pain. Manual handling can effect in fatigue, and lead to injuries of the back, neck, shoulders, arms or other body parts. Thus, ergonomic workstation and working posture plays an important role to avoid those disorder and risk. A conceptual framework for integrating ergonomics into designing sustainable work systems effectively to eliminate the health hazards has been proposed [3]. The discomfort feel by worker will also reduce working efficiency. Finally, productivity of worker greatly depends upon ergonomic design of workstation [3].

Although nowadays there are automatic techniques that have been employed in manufacturing industries to increase productivity and efficiency, there are still lots of manual handling jobs, especially for assembly and maintenance jobs. Due to incorrect or awkward working posture, the workers may be exposed to various ergonomics risk factors (See Table 1). The workers usually feel discomfort at their low back pain and experienced overall muscle fatigue as well. Other than that, the workers enthusiasm will be affected since they suffered from the pain and would affect the productivity. Figure 1 shows the recommended space for comfortable working reachable area for a worker,

Table 1 Bottleneck Factors Analyzed by Motion Study

Factor	Illustration	Description	Reasons
1. Bending Effect on: back and neck		Too much neck bending to carry out the task.	Height of workstation is less
2. Stressed body reach Effect on: shoulder and waist		Improper reaching of parts since workstation design causes stressed body movements.	Poor workplace design and less awareness of body posture.

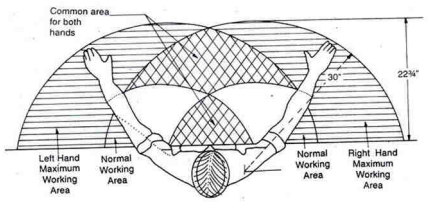

Figure 1 Maximum Working Area of Shoulders

2. METHODOLOGY

Several methodologies were used in this research.

1. Questionnaire - At the insert folding workstation, the ergonomic features that are needed by the operators are determined by questionnaire surveys. The survey conducted among the operators at the insert folding process area. Five operators were involved in this survey to collect the required information.

2. Testing and Analysis - The data that has been collected from the company is been analyzed and calculated by using House of Quality, CATIA V5 and RULA analysis. Redesign of the workstation is required to improve the RULA score which is directly reduced the musculoskeletal disorder. Solidwork software was used to analyze the finite element of product
3. Recorded video - By using recorded video, operators were observed of how they operate the work. From observation, the awkward postures can be seen experienced by workers during working. Worker frequently over-reaching their hands forward.

3. RESULTS AND DISCUSSION

House of Quality (Figure 2) were constructed in order to gain valuable insights to move forward with the research. Suitable height of workstation and ergonomic posture got the highest scores for engineering requirement factors to be improvised.

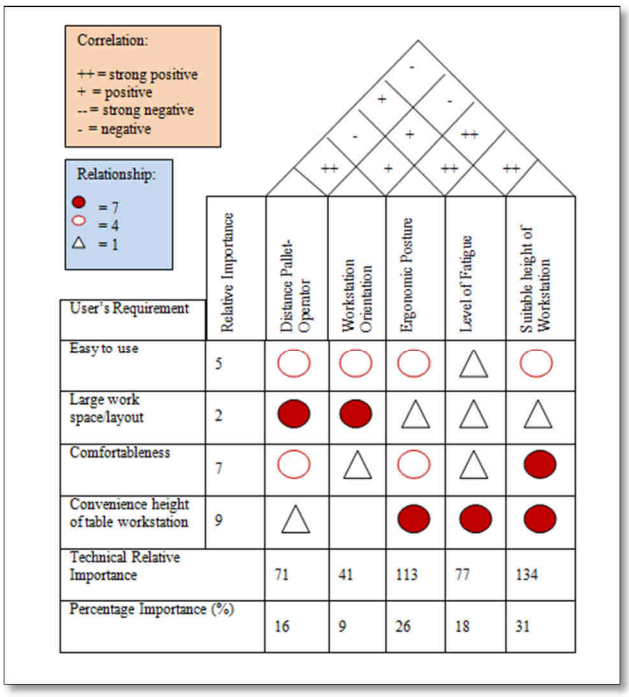

Figure 2 House of Quality

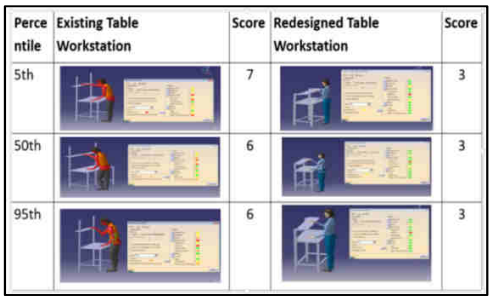

Figure 3 Comparison of RULA Analysis between existing and redesigned workstation

RULA analysis using CATIA V5 (Figure 3) was done to identify areas with ergonomics problems and ways to correct it. After analysis, the redesign table workstation is more ergonomic, able to reduce pain and uncomfortable feeling. The RULA Analysis score was reduced to 3 from 6 (see Table 2). The redesign table workstation with extra feature of adjustability can greatly improve working posture of the manual handling worker.

Table 2 Score range in RULA analysis

Final Score	Description
1 and 2	Posture is acceptable if it is not maintained for long periods.
3 and 4	Further investigation may be required.
5 and 6	Investigation and changes are required soon.
7	Investigation and changes are required immediately

4. CONCLUSION

Fatigue has been identified as a causing factor for accidents, injuries and death in a wide range of settings, with the effects that tired people are less likely to produce safe judgment and actions. This research has managed to suggest improvement to the management of the company to improve the condition of workstation. This in turn reduce ergonomic problems faced by workers and improve working satisfaction.

5. REFERENCES

[1] A. Williamson, D. A. Lombardi, S. Folkard, J. Stutts, T. K. Courtney, and J. L. Connor, "The link between fatigue and safety," *Accid. Anal. Prev.*, vol. 43, no. 2, pp. 498–515, 2011.

[2] C. R. Dickerson, K. a. Meszaros, A. C. Cudlip, J. N. Chopp-Hurley, and J. E. Langenderfer, "The influence of cycle time on shoulder fatigue responses for a fixed total overhead workload," *J. Biomech.*, vol. 48, pp. 2911–2918, 2015.

[3] A. Radjiyev, H. Qiu, S. Xiong, and K. Nam, "Ergonomics and sustainable development in the past two decades (1992–2011): Research trends and how ergonomics can contribute to sustainable development," *Appl. Ergon.*, vol. 46, pp. 67–75, 2015.

Application of right leg drive topology in an EMG acquisition circuit

Z. Fu[1,*], A.Y. Bani Hashim[1], Z. Jamaludin[1], I. S. Mohamad Jamaludin[2]

[1)]Department of Robotics & Automation, Faculty of Manufacturing Engineering,
UniversitiTeknikal Malaysia Melaka,HangTuah Jaya, 76100 Durian Tunggal, Melaka, Malaysia.
[2)] Department. of Thermal-Fluid, Faculty of Mechanical Engineering,
UniversitiTeknikal Malaysia Melaka, Hang Tuah Jaya, 76100 Durian Tunggal, Melaka, Malaysia.

[*]Corresponding e-mail: zinvifu@yahoo.com
Keywords: Electromyography; right leg drive; common mode signal

ABSTRACT – The right leg drive (RLD) circuit is an effective strategy in reducing the common mode noise of biopotential signals. In this study, we aim to determine the relevance of the RLD circuit to the acquisition of EMG signals. To examine the performance of the RLD circuit with EMG signals, the resulting common mode signal was compared with and without the RLD. Our results indicate that for EMG acquisition, grounding the CM mode signal provided better CMRR because the RLD can cause distortion to the common mode signal. We therefore conclude that as far as the EMG is concerned, the RLD does not necessarily improve CMRR performance and also adds complexity to the overall circuit.

1. INTRODUCTION

Biopotential signals are electromagnetic waves produced within the body. Although there are various biopotential signals (e.g., Electroencephalography (EEG), Electrocardiography (ECG) and Electromyography (EMG), their acquisition method are fairly similar, which is by means of a differential amplifier, followed by subsequent filtering and amplification. EMG signals from skeletal muscles can be obtained on the skin surface with surface electrodes.

However, these EMG signals are small and contaminated with unwanted electric noise, the biggest issue being the 50/60Hz interference from the power line. Equation (1) describes the signal acquired, S*(t)* on the skin as a sum of the EMG $E_{EMG}(t)$signal itself and other interferences, $E_{cm}(t)$, $E(t)$, $B(t)$, $Rf(t)$ are the common mode power line, electric, magnetic and radio frequency interferences while V_{dc} is the dc offset voltage due to electrodes and component tolerance.

$$S(t) = E_{EMG}(t) + E_{cm}(t) + E(t) + B(t) + Rf(t) + V_{dc} \quad (1)$$

In this experiment, eliminating the E_{cm} is of particular interest as it is the biggest contributor of noise in a biopotential amplifier. There are a few methods to reduce the common mode signal. First, the differential amplifier within an instrumentation amplifier effectively reduce the noise by 80-120dB. A second tier common mode reduction can be achieved by passive grounding having the purpose of fixing the subject voltage under the ground electrode as equal to that of the isolated ground[1], or by negative feedback where the common mode signal is inverted, amplified and fed back to the body as a correction signal to minimise the common mode itself. The different topologies of these methods are shown in Figure 1.

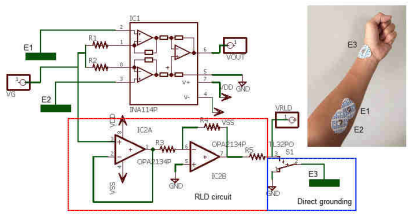

Figure 1 Single EMG acquisition circuit designed for quick switching between RLD and direct grounding

The RLD has been used in many designs especially in ECG acquisition [2-3]. As opposed to ECG, EMG acquisitions normally are directly grounded, however some EMG circuit designs also use the RLD [4-5]. There are no issue with applying RLD on EMG acquisition due to the similarity of the circuit and the targeted signal. However to date, whether the EMG circuit would really benefit from the RLD, is still a subject of study.

2. METHODOLOGY

The experimental setup is also shown in Figure 1. The INA114 instrumentation amplifier was used with two gain resistors of 2400Ω connected in series provide a gain of 100. Two electrodes, E1 and E2 were placed over the flexor digitorum superficialis muscle (FDS) and a third electrode, E3 which was switched between the direct grounding and the right leg drive circuit. The electrodes were connected to the instrumentation amplifier with a shielded cable of 1.5m. Readings were taken from the INA output, V_{out}, the common mode voltage tapped from the gain resistors output, V_G and the RLD output, V_{RLD}. When the subject flexed the forearm, the FDS muscle output was acquired. The data was acquired with the National Instruments NI-cDAQ 9178 data acquisition unit with the NI9205 module, sampled at 1 kHz.

3. RESULTS AND DISCUSSION

The result of circuit simulation with TINA is shown in Figure 3. In the simulation, a 200mV signal was extracted from a 10Vpp CM noise. From the simulation results, it can be seen that while direct grounding already provided an acceptable CMRR, the RLD was capable of further noise reduction.

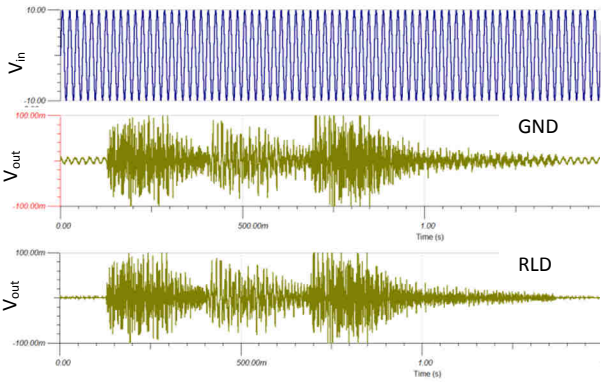

Figure 2 Simulation results of test circuit. Top: input signal, centre: direct grounding, bottom: RLD

Figure 3 shows the common mode noise in V_{out}. The result of grounding provided the lowest level of baseline noise, compared to using the RLD. The result floating the ground causes V_{out} to increase to $0.9V_{pp}$. In Figure 4,

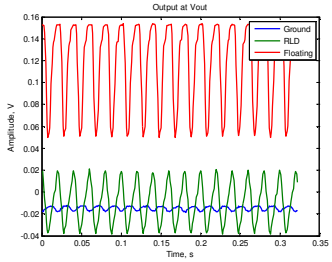

Figure 3 Common mode noise amplitude at V_{out}, blue: direct ground, green: RLD, red: floating

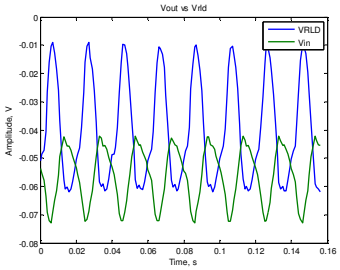

Figure 4 Comparison of V_{RLD} (blue) and V_{in} (green), showing a degree of distortion to the original signal

V_{RLD} which was negative amplified is compared against the original input common mode signal. Ideally V_{RLD} should mirror V_{in}, however in this case, there is a phase shift of approximately 5° and a considerable distortion in shape compared to V_{in}. Since the feedback signal is not identical to the common mode signal, cancellation is not effective. In Figure 5, the overall effect of using grounding and the RLD can be observed. The ground method provided better CMRR (72%) compared to using the RLD (47%).

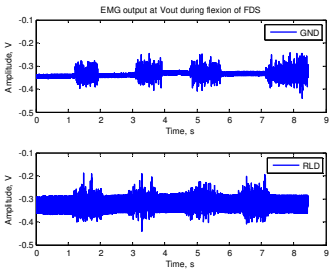

Figure 5 EMG output for FDS flexion, top: Ground, bottom RLD

A few contributing causes to the poor common mode of the RLD has been identified. First, the distortion shown in Figure 2 may be caused by stray capacitance within the RLD path. Next, common mode coupling also interferes at the cable, due to its length. A shorter cable would result a better CMRR.

4. CONCLUSION

We can conclude that the RLD circuit is not straightforward to implement. In the case of a priority for simple EMG circuits, the grounding method is adequate for CM reduction. In our case the RLD does not provide additional CMRR as expected. Although it is possible to optimize the RLD loop performance, additional components will be needed.

ACKNOWLEDGEMENT

This research is supported by the Malaysian Ministry of Education, research grant identification number FRGS/2/2013/SG02/FKP/02/2/F00176.

REFERENCES

[1] T. Koshio, S. Sakurazawa, M. Toda, and J. Akita, "Identification of Surface and Deep Layer Muscles Activity by Surface EMG," *SICE Annu. Conf.* 2012, pp. 1816–1821, 2012.

[2] C. S. Wang, "A new AC-coupled amplifier for portable ECG without reference electrode," *Comput. Electr. Eng.*, vol. 39, no. 1, pp. 141–149, 2013.

[3] E. M. Spinelli, R. Pallàs-Areny, and M. A. Mayosky, "AC-coupled front-end for biopotential measurements," *IEEE Trans. Biomed. Eng.*, vol. 50 (3) pp. 391–395, 2003.

[4] M. H. Khan, A. Wajdan, M. Khan, H. Ali, J. Iqbal, U. Shahbaz, and N. Rashid, "Design of low cost and portable EMG circuitry for use in active prosthesis applications," 2012 *Int. Conf. Robot. Artif. Intell. ICRAI* 2012, pp. 204–207, 2012.

[5] J. Kim, S. Mastnik, and E. André, "EMG-based hand gesture recognition for realtime biosignal interfacing," in *Proceedings of the 13th international conference on Intelligent user interfaces - IUI '08*, 2008, pp. 30–39.

Nanostructured iron oxide by thermal oxidation

F.I.A. Bakar, S. Ismail*, J.A. Razak

Carbon Research Technology Research Group, Engineering Materials Department, Faculty of Manufacturing Engineering, Universiti Teknikal Malaysia Melaka, Hang Tuah Jaya, 76100 Durian Tunggal, Melaka, Malaysia

*Corresponding e-mail: syahriza@utem.edu.my

Keywords: Iron oxide; Thermal oxidation; Hematite

ABSTRACT - Oxidation of iron foil in atmospheric condition was studied to obtain the optimum formation condition of nanostructured iron oxide. The composition of oxidation products were analyzed by XRD and Raman characterization tools. While, FESEM observation had shown that the Fe_2O_3 nanostructure was formed on pure Fe substrate. The oxidation product at higher temperature of 600°C yielded that the hematite was presence as the dominant phase. While, at 400°C, magnetite was appeared on the Fe foil and above that temperature, Raman spectra results had shown the presence of hematite in the outer oxidation layer. Growth of nano-hematite on Fe foil influences a surface diffusion mechanism that controlled by the heating duration factor.

1. INTRODUCTION

Metal oxide is stable material phase than metallic counterparts in an oxidative environment. Recently, iron oxide nanostructures have been synthesized by various methods which normally involved with three major phases. From the liquid phase (hydrothermal, electrodeposition), from the gas phase (chemical vapor deposition) and solid phase (thermal oxidation). Nevertheless, thermal oxidation in various oxidizing atmosphere is a most simple, cheap, and direct procedure to form hematite (α-Fe_2O_3) [1]. The growth of nanostructure on the surface of iron is based on their oxidation variables. Under typical conditions, different layer of oxides will be formed simultaneously, which are hematite, magnetite and wustite. Hematite (Fe_2O_3) is formed the outer layer while magnetite (Fe_3O_4) at intermediate layer and wustite (FeO) layer form on an iron substrate [2]. Hematite (α-Fe_2O_3) is the most common form of crystalline iron oxide with preferred growth direction along the [110] planes and typically red in color. Furthermore, hematite (α-Fe_2O_3) are more stable with a full set of functional properties and become as a strong candidate material for photo conversion of light to electric energy as it possesses a bandgap (Eg = 2.1eV), high chemical stability, and superior against corrosion [3-4]. However, in this study, the feasibility of simple thermal oxidation of iron substrate to produce nanostructured hematite was examined. The growth mechanism is justified based on the morphological observation and the spectroscopy analysis. By exploiting the structured resulting from this simple approaches, the enhance properties of hematite can be reaped for various promising applications such as photoanode, pigments, catalyst, flocculants, wastewater treatment absorbents and so on [5].

2. METHODOLOGY

High-purity iron foil (99.99%) was used with thickness of 0.25 mm in the oxidation experiment. The substrate was cut into desired shape with dimension of 3.0 x 0.5 cm. Next, the foils are rinsed with deionized water by sonication in ethanol for 10 min. Then, the cleaned Fe substrate is dried in an air stream and placed on a substrate heater in chamber furnace. The furnace is then sealed and Fe samples are heated around 200°C to 600°C and cooled down at room temperature at rate ~10°C min^{-1}. The oxidation was held for 90 and 120 minutes. All parameters selected were referring from the previous study by Ismail et al., [6]. A field emission scanning electron microscope (FE-SEM, S4800, Hitachi), are used to evaluate the growth morphologies. The structural characteristics of nanostructure were identified by X-ray diffraction (Bruker Axs D8 Advance) using CuKα radiation and Raman spectrometer (UniRAM-3500) that was performed at a laser wavelength of 532 nm.

3. RESULTS AND DISCUSSION

Figure 1 (a-c) depicts the FESEM images at the top surface of nanowire layer on Fe substrate that were oxidized at the temperature of 200 to 600 °C. Figure 1 (a) ii -(c) ii are magnified images of Figure (a) i -(c) i. As seen in Figure 1 (a), at 200°C the formation of nanostructure are not formed on the substrate. This is due to insufficient heat supplied for an oxidation to execute. The expose temperature is below than oxidation temperature of iron (Fe). On the other hand, the morphological observation has indicated the growth of nanowires on the surface of iron substrate when oxidation temperature is 400 °C (Figure 1 (b)). At 400°C the physical observation indicates the oxidized samples are disintegrated and the majority area of oxidized sample had turned into red color. While, at temperature above 600°C, nanorod structure is produced as seen in Figure 1 (c) and the bottom part of the substrate is consolidated that because of formation of short nanowires. Only the longer nanowires are survived. Thus only a few strands of nanowires are seen on the substrate. This is due to the diffusion process of substrate which occurs at the higher rate. Higher activated energy on the grain boundary and active crystallographic plane of [110] was contributed to the growth of nanostructure on the substrate [6]. Therefore, the whole sample had turned into grey color and it was completely oxidized. Based on Figure 1 (a-c), the nanowires that were formed become coarser with increasing reaction temperature, indicating the obvious temperature effect on the morphologies development of the nanostructures.

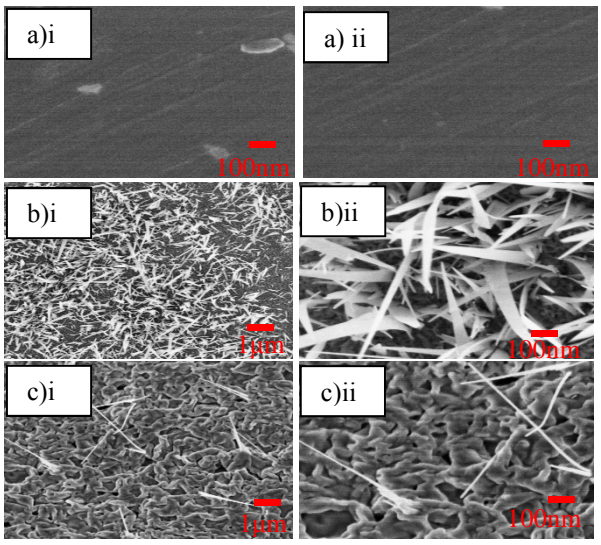

Figure 1 FESEM image of the iron substrate oxidized at 90 min (a) 200°C, (b) 400°C and (c) 600°C

The Raman spectrum of the as-prepared sample is shown in Figure 2. From the Raman shift, at temperature 400°C and 600°C, the phase appeared are; α-Fe_2O_3 and Fe_3O_4. There are seven major peaks presented, located at 225, 245, 292, 411, 496, 612, and 660 cm^{-1} which correspond to the α-Fe_2O_3. Two Raman modes, A_{1g} modes (225 and 496cm^{-1}) and E_g modes (292, 411 and 612 cm^{-1}) are seen in this spectra. The peaks located at 660 cm^{-1} which corresponds to the Fe_3O_4. This result is matched with Zhong et al., [7]. From the spectra, as the temperature was increasing, only single phase of α-Fe_2O_3 are been detected. This is due to phase transition during an oxidation process and their related grain growth phenomena. Furthermore, the new grain formation may influence during an oxidation process. The intensity of hematite was increased with an increasing of oxidation time.

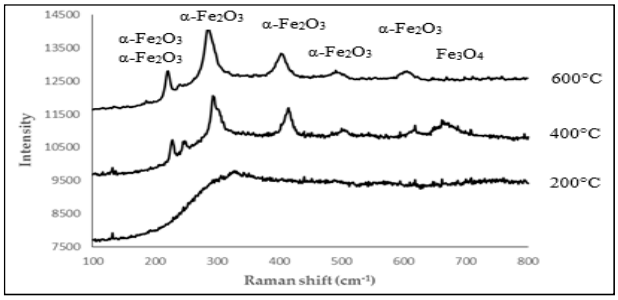

Figure 2 Raman spectrum for the sample heated at various oxidation temperature within 90 minutes

Figure 3 shows the XRD pattern of the as-prepared samples obtained at different temperature. Two phases of iron oxide, Fe_3O_4 and α-Fe_2O_3 were formed by heating the Fe substrate in air from 400°C. These two phases are stable at room temperature [5]. Furthermore, as the temperature increased, the peak from iron substrate are disappeared on substrate due the substrate was fully covered by an oxide layer. The peak correspond to α-Fe_2O_3 with lattice constant of a = 0.5009 nm and c =1.364 nm (JCPDS file No. 01-072-6226) as confirmed by the XRD pattern. The XRD pattern of the α-Fe_2O_3 nanowires exhibits a much higher intensity ratio of the (110) plane diffraction peak than intensity of the (104) plane. This may indicate a favorable growth direction of the nanowires formation.

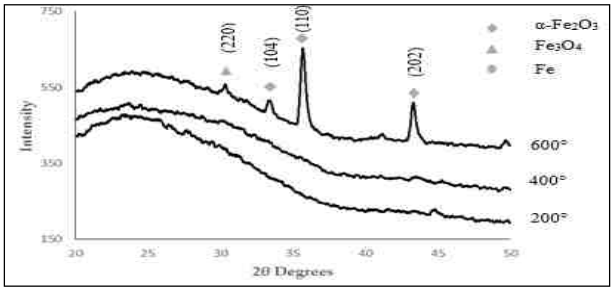

Figure 3 XRD patterns for iron foil heated at different temperatures

4. CONCLUSION

As the conclusion, α-Fe_2O_3 layer with ordered nanostructure were successfully formed on pure Fe foils by using thermal oxidation technique in air at constant time with various range of exposing temperature at 200°C to 600°C. In term of α-Fe_2O_3 nanowires formation, as time increase, nanostructures change from nanoleaf to nanowire formation and the dimensional width of nanostructure are becoming smaller.

ACKNOWLEDGEMENT

This work was supported by the Short Term Research Grant UTeM (PJP/2014/FKP (4A)/S01350) and (FRGS /2/2014/TK04/FKP/03/F00241).

REFERENCES

[1] S.Grigorescu, C-Y.Lee, K.Lee, S.Albu, I.Paramasivam, L.Demetrescu, and P. Schmuki, "Thermal air oxidation of Fe: rapid hematite nanowire growth and photoelectrochemical water splitting performance," *Electrochemistry Communications*, vol. 23, pp. 59-62, 2012.

[2] M. Marijan, M. Ristic, M. Ivanda, and S. Music,"Formation of iron oxides by surface oxidation of iron plate," *Croatica Chemica Acta*, vol. 85, no. 1, pp. 117-124, 2012.

[3] Y. Fu, J. Chen, and H. Zhang, "Synthesis of Fe_2O_3 nanowires by oxidation of iron," *Chemical physics letters,* vol. 350, pp. 491-494, 2001.

[4] Q. Han, Y.Y. Xu, Y.Y. Fu, H. Zhang, R.M. Wang, T.M. Wang, and Z.Y. Chen, "Defects and glowing mechanisms of α-Fe_2O_3 nanowires," *Chemical physics letters*, vol. 431, no. 1-3, pp. 100-103, 2006.

[5] X. Wen, S. Wang, Y. Ding, Z.L. Wang, and S. Yang, "Controlled growth of large-area, uniform, vertically aligned arrays of α-Fe_2O_3 nanobelts and nanowires," *Wen, Xiaogang,* vol. 109, no. 1, pp. 215-220, 2005.

[6] S. Ismail, N. S. Saad, and J. A. Razak "Nanostructured Hematite Prepared by Thermal Oxidation of Iron," *In Key Engineering Materials,* vol. 694, pp. 208-212, 2016

[7] M. Zhong, Z. Liu, X. Zhong, H. Yu, and D. Zeng "Thermal growth and nanomagnetism of the quasi-one dimensional iron oxide," *Journal of Materials Science & Technology,* vol. 27, no. 11, pp. 985-990, 2011.

Development of steward platform-based for ankle muscle rehabilitation

N. S. Razali[1], R. Ghazali[1,2,*], S.Y.S. Hussien[1,2], H.I. Jaafar[1,2], M.Z.A. Rashid[1,2]

[1)]Faculty of Electrical Engineering, Universiti Teknikal Malaysia Melaka,
Hang Tuah Jaya, 76100 Durian Tunggal, Melaka, Malaysia.

[2)]Center for Robotics and Industrial and Automation, Universiti Teknikal Malaysia Melaka,
Hang Tuah Jaya, 76100 Durian Tunggal, Melaka, Malaysia.

[*]Corresponding e-mail: rozaimi.ghazali@utem.edu.my

Keywords: Steward platform; PID controller; robotic rehabilitation

ABSTRACT – Sore muscle is a common symptom happens after post-workout. While, pulled muscle or a torn muscle is categorized as muscle injury which cause muscle weakness and reduces performance of muscle. Thus, rehabilitation is needed in order to re-energize the performance. This paper presents a degree-of-freedom (6-DOF) Steward platform-based designed for ankle exercise. In this study, there are several lower limb muscle will be focused on. The posterior and anterior muscle activates when the ankle moves. LabVIEW software was used as a host target and platform interface. The platform was analyzed based on its motor performances which optimized by auto-tuned PID controller. The comparative assessment of the transient response between simulation and experiment is presented and discussed.

1. INTRODUCTION

Since the increasing trends of the elderly society, the essentials of health care and rehabilitation must be taking into consideration. The idea of rehabilitation robot may contain a wide range of mechatronic tools to support rehabilitation session in medical centre. Robotic rehabilitation can replace the training effort by therapist, spend a reasonable cost to perform a therapy and observe the level of motor recovery by measuring the performances

Steward platform is one of the parallel robots that have been developed. It consists of six actuator's interaction and coordination which is called as six degree-of-freedom (6-DOF). There are many control method have been proposed in order to control the platform movement. Proportional-Integral-Derivative (PID) controller is a potential controller that can control the platform.

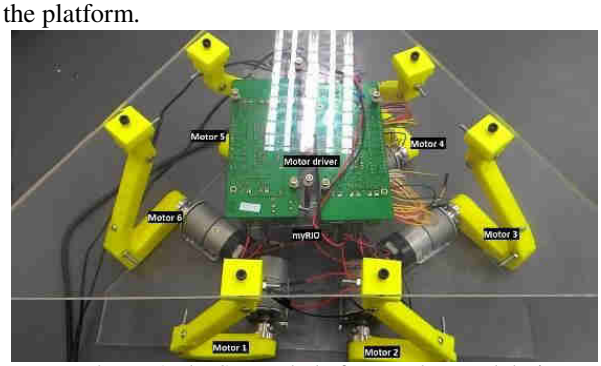

Figure 1 The Steward platform and control design

2. METHODOLOGY

2.1 Steward platform and control design

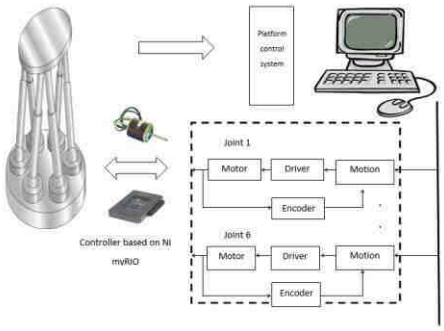

Figure 2 The Steward platform and control design

Figure 2 shows the operation of Steward platform which is controlled by myRIO. The system consists of six independent loops or joints under robot control model. This model receives a command created in LabVIEW to perform motor operation based on the position receives by encoders. A myRIO acts as data acquisition which has 10 analogue inputs, six analogue outputs and 40 digital inputs/outputs line. A platform control system represented as a host target. All of the data collected can be illustrated directly through the graphical user interface.

2.2 Monitoring platform angle projection

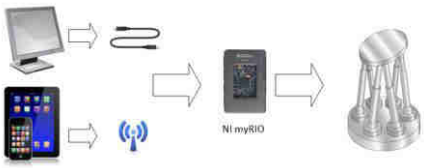

Figure 3 GUI monitoring

Based on Figure 3, the platform angle projection can be chosen directly from the graphical user interface provided. This platform can be moved in 6-DOF which is in *x*-axis direction, *y*-axis direction, *z*-axis direction, roll, pitch and yaw. The Steward platform can be controlled by using either USB configuration or Wi-Fi configuration. If Wi-Fi configuration is used, myRIO must be set up with a valid internet protocol (IP) address. Otherwise, myRIO cannot be synchronized with the host target. On the host target, there are a toolbar provided in order to move the platform based on the range of motion that was set up in the programming.

2.3 *Platform Range of Motion*

Basically, the muscle that affected from this movement is knee muscles which are quadriceps and hamstrings. However, this research concentrates only at the ankle muscle. There are six platforms of angle projection which are *x*, *y* and *z*-axes, roll, pitch and yaw platform. The roll movement is similar to the ankle range of motion which is plantar flexion and dorsiflexion. Besides, pitch movement which is defined as inversion and eversion of the ankle rotate on *y*-axis while yaw is the rotation on *z*-axis. Clinically, the movement for the ankle called as external rotation (abduction) and internal rotation (adduction). The angle for each motor is tabulated in order to ensure the platform moves in 6-DOF as in Table 1.

Table 1 Platform of angle projection [1]

Motor	1	2	3	4	5	6
***x*-axis**	45˚ to 15˚	15˚ to 45˚	20˚	45˚ to 15˚	15˚ to 45˚	20˚
***y*-axis**	20˚	20˚	0˚ to 40˚	40˚ to 0˚	40˚ to 0˚	0˚ to 40˚
***z*-axis**	0˚ to 40˚	0˚ to 40˚	0˚ to 40˚	0˚ to 40˚	0˚ to 40˚	0˚ to 40˚
Roll	45˚ to 0˚	0˚ to 20˚	0˚ to 20˚	0˚ to 20˚	45˚ to 0˚	45˚ to 0˚
Pitch	35˚ to 0˚	35˚ to 0˚	0˚	0˚ to 18˚	0˚ to 18˚	0˚
Yaw	0˚ to 18˚	25˚ to 0˚	0˚ to 18˚	25˚ to 0˚	0˚ to 18˚	25˚ to 0˚

3. RESULTS AND DISCUSSION

3.1 *System Optimization*

The response data for each motor which connected at the Steward-platform are collected. The obtained transfer function had been validated by comparing the motor model (simulation) with the actual motor model (experiment) with sampling time of 0.01 second. The transfer function for each motor is tabulated in Table 2.

Table 2 Motor transfer function

Motor	Transfer function
1	$G(s)=\frac{6.516s^2+0.7296s+8.706}{s^3+0.1591s^2+1.034s+0.01425}$
2	$G(s)=\frac{6.32s^2-0.439s+7.898}{s^3+0.03695s^2+0.9698s+0.00152}$
3	$G(s)=\frac{7.334s^2+8.932s+5.462}{s^3+0.09462s^2+0.6219s+0.001008}$
4	$G(s)=\frac{8.011s^2+1.741s+7.65}{s^3+0.2572s^2+0.8734s+0.001889}$
5	$G(s)=\frac{6.914s^2+0.2693s+10.75}{s^3+0.455s^2+1.192s+0.00296}$
6	$G(s)=\frac{7.77s^2+2.773s+4.804}{s^3+0.3516s^2+0.5688s+0.007417}$

The Steward platform is optimized by auto-tuned PID controller in order to obtain the proportional gain (K_p), integral gain (K_i), derivative gain (K_d) and filter coefficient (N) shown in Equation (1). The parameters of PID controller are tabulated in Table 3.

$$PID = K_p + K_i\frac{1}{s} + K_d\frac{N}{1+N\frac{1}{s}} \quad (1)$$

Table 3 Parameters of PID controller

Motor	Auto-tuned PID			
	K_p	K_i	K_d	N
1	1.50	0.17	0.16	14.50
2	1.29	0.12	0.15	12.31
3	1.11	0.27	0.17	9.97
4	2.82	0.46	0.21	17.17
5	1.39	1.03	0.17	14.53
6	1.92	1.27	0.20	16.97

Figure 4 shows the comparison response in Steward platform between simulation and experiment. The transient response of Steward platform which optimized by auto-tuned PID controller improved the overshoot (OS), settling time (T_s) and rise time (T_r) compared to the response before optimized with any controller. The comparison of transient response between before optimization and after optimization is tabulated in Table 4.

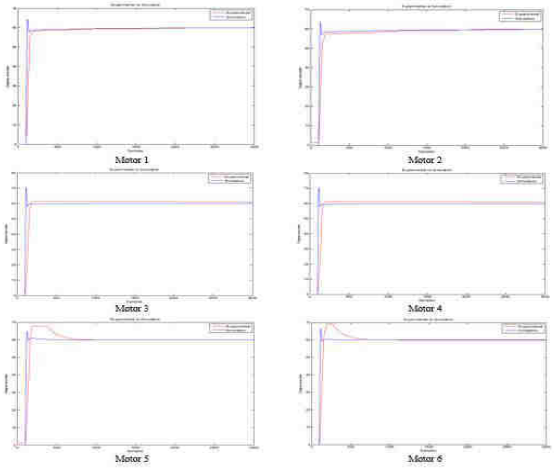

Figure 4 Motor performances

Table 4 Comparison of motor performances

Motor	Before Optimization			After Optimization		
	OS (%)	T_S (s)	T_r (s)	OS (%)	T_S (s)	T_r (s)
1	15.70	0.94	0.19	8.63	0.32	0.11
2	18.50	1.05	0.20	9.18	0.39	0.12
3	19.10	1.08	0.20	9.04	0.41	0.13
4	17.50	0.97	1.19	11.30	0.42	0.12
5	17.30	0.96	0.19	10.60	1.60	0.11
6	13.50	0.68	0.20	10.10	1.32	0.09

4. CONCLUSION

A platform based ankle rehabilitation robot is developed through Steward platform for the patients who are suffered from injuries and muscle fatigues. In this research, the transient response of Steward platform controller by PID controller optimized by auto-tuned shows a better performance compared to the before optimized. In the future, a Wi-Fi nunchuck remote will be used to control the platform movements. An electromyography (EMG) also will be attached in order to evaluate muscle potential.

REFERENCES

[1] American Academy of Orthopaedic Surgeons, *Joint Motion: Method of Measuring and Recording*, USA: Churchill Livingstone, 1965.

Design and development of roof for covering car

Z. Abdullah[1*], M.R. Raduan[1], H.Y. Ting[1], M.M. Ghazaly[2], M.S. Kasim[1], S. Maidin[1].

[1)] Faculty of Manufacturing Engineering, Universiti Teknikal Malaysia Melaka, Hang Tuah Jaya, 76100 Durian Tunggal, Melaka, Malaysia

[2)] Faculty of Electrical Engineering, Universities Teknikal Malaysia Melaka

[*]Corresponding e-mail: zulkeflee@utem.edu.my

Keywords: AHP approach, SolidWork software, Product design

ABSTRACT – A protective covering for the vehicle is specifically mountable on an outside surface of a vehicle. The car cover is used for slowing or reducing the rate of heat build-up in an interior compartment of a car is disclosed. Therefore, this research had focused on optimizing and develop the design concept of roof for covering car based on influence factor. The design selection process was implemented to finalize the best design by applying Analytical Hierarchy Process Method (AHP). The best final design concept proceeded with design stage and the simulation analysis part is done by using the SolidWork 2013 software.

1. INTRODUCTION

The Covering Car is the option can be used to cover the car from corrosion, maintain interior cool, and protect the dash, other interior surfaces from extreme heat and possible harmful effects of the sun. However, many of these devices [1-2] are directed mainly to protecting the body of the car, rather than maintaining the interior of the car cool during temporary parking of the car in the hot sun. Therefore, the purpose of this project is to develop and design the component of Roof for Covering Car.

The garage is not enough to protect our car or vehicle, sometimes our car is kept outside sitting exposed to the element all year round. Strong UV rays from the baking summer sun beat down onto exposed vehicle exteriors, fading the paintwork, trim rubber parts.

Roof of Covering Car is the new idea for the accessory of vehicle that attach at the roof of the vehicle without reducing the interior space for occupants. This is more suitable for a long period when park under the sunshine, which compare to other car cover in the market nowadays. Figure 1 shows the example of car covers concepts. It also can be used for aesthetic quality for hanging around or fun purpose while using the fancy looking car cover at the roof. Furthermore, this product uses the mechanical component so that the user can easily pulls the roof from the housing to cover the car.

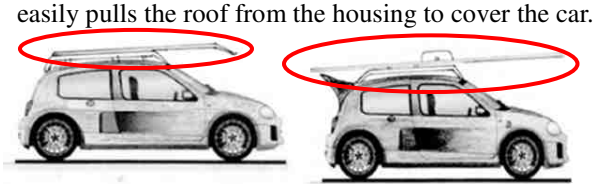

Figure 1 Example of car covers concepts

2. METHODOLOGY

The procedures and the workflow are discussed in this section. Therefore, the planning process is built by using the flow chart. It is so important to understand the whole methodologies that are used in order to design and develop roof for covering car. The sequence of processes is shown in Figure 2.

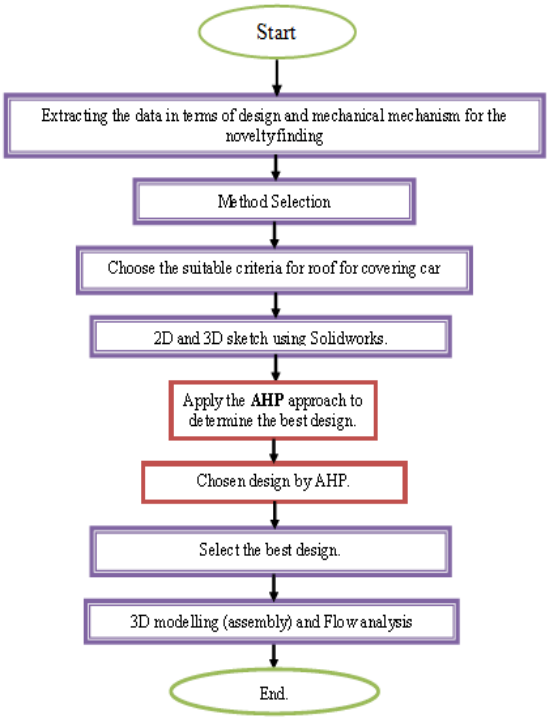

Figure 2 Flow chart of design and development

A design concept is an idea for a design. Several designs has been proposed and the best design was chosen by using AHP [3] and Integrated approach. Material selection methodology and design modeling are used as a part of this examination. Ashby [4] mentioned that there are four basic steps in material selection, which are translated, screening, ranking and supporting information. Design is the process whereby the product was created and modified, consisting all activities associated from the original concept to finished product. The final design was designed by using SolidWork software.

3. RESULTS AND DISCUSSION

Several designs had been proposed and the final best design was chosen by using Analytical Hierarchy Process (AHP). The best final design was modeled in three- dimensional (3D) and will test on flow simulation analysis by using SolidWork software.

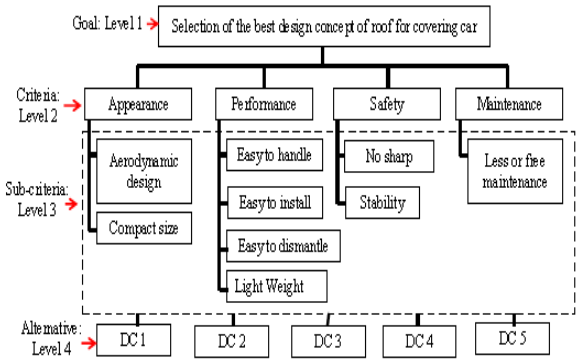

Figure 3 A hierarchical model for the selection of design concept [2]-[5]

Each element is compared by using the relative scale pairwise comparison. The average of normalized (ANC) method is used to calculate the vectors of priorities and result for this calculation is summarized. To make sure the judgments are consistency verification is incorporated in order to measure the degree of consistency among the pairwise comparisons by computing the consistency ratio and summarizes it. As the value of consistency ratio for all sub-criteria and alternatives is less than 0.1, the judgments are acceptable.

Table 1 shows the design concept 5 (DC5) has the highest value for further development. The second highest is the design concept 1 (DC1) and the lowest value or last choice is the design concept 4 (DC4). Design concept 5 is preferred choice since it has the highest value among five alternatives. Figure 4 shows the concept design of the car development.

Table 1 Result of selection

DC1	0.23130
DC2	0.19691
DC3	0.17387
DC4	0.15571
DC5	0.24217

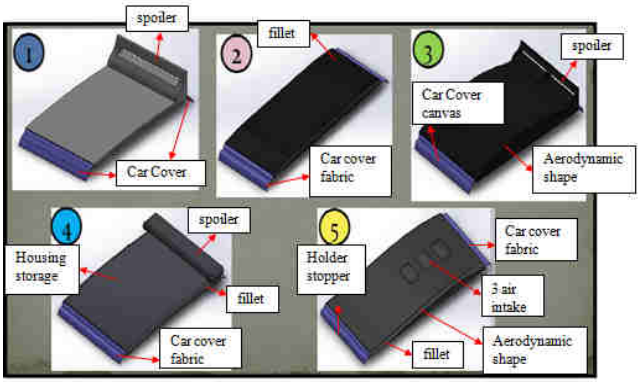

Figure 4 Concept designs

Material selection was done by using CES Edupack software based on four stages, translation, screening, ranking, and documentation to obtain more accurate results. The materials selected for each part of a roof for covering car depend on the design requirement in order to select the best material for each of this part. Table 2 described the design requirement for a body cover.

Table 2 Design requirements for body cover

Function	To make a body cover for roof for covering car
Objective	Minimize cost
Constraints	Corrosion resistance
	Water proof
	Light weight
	Easy to fabricate
	Good surface finish
Free variable	Choice of material

SolidWork Flow Simulation allows to graphically display the reaction of velocity and pressure that act on any part in the flow simulation. The flow simulation analysis was done by using SolidWork 2013 software to evaluate the flow trajectories on body car cover. The analysis result shows that there is no turbulences front and behind the body cover and there is no collision behind the body cover with the air flow from below (see Figure 5).

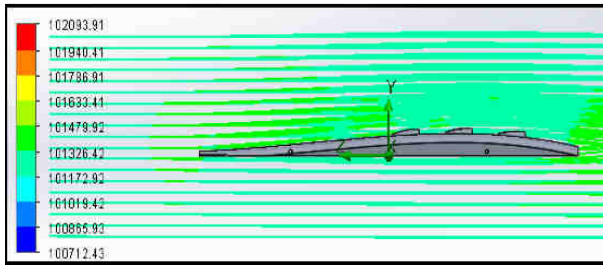

Figure 5 Flow trajectories on body car cover

4. CONCLUSION

In conclusion, the objective is achieved in order to optimize the conceptual design which are generating the new design concept of roof for covering car based on influence factor that was identified. Then, the best conceptual design roof for covering car is chosen by using Analytical Hierarchy Process (APH) approach. The result shows that the best final concept that has been selected which is concept 5 because it has higher priority value among the other conceptual design.

REFERENCES

[1] Matthew B. Porter. (1993). (12) United States Patent. 2(12).

[2] Suh, T. J., & Angeles, L. (2011). (12) United States Patent. 2(12).

[3] Saaty, T.L., 1980. *The Analytic Hierarchy Process*, New York: McGrawHill.

[4] Ashby, M F., 2011. *Materials Selection in Mechanical Design*, 4thed, China: Elsevier Ltd

[5] Hambali, 2009. International Journal of Mechanical and Materials Engineering. *Composite Manufacturing Process Selection Using Analytical Hierarchy Process*. 4 (1)

Tracking performance of nonlinear proportional-integral-derivative for XY table ballscrew drive system

S.C.K. Junoh[1,*], S.H. Ooi[1], L. Abdullah[1], S.N.S. Salim[2], N.A. Anang[1], T.H. Chiew[1], Z. Retas[3]

[1)] Faculty of Manufacturing Engineering, Universiti Teknikal Malaysia Melaka, Hang Tuah Jaya, 76100 Durian Tunggal, Melaka, Malaysia
[2)] Faculty of Engineering Technology, Universiti Teknikal Malaysia Melaka, Hang Tuah Jaya, 76100 Durian Tunggal Melaka
[3)] Department of Electrical Engineering, Politeknik Merlimau, KB 1031 Pej. Pos Merlimau, 77300 Melaka, Malaysia

[*]Corresponding e-mail: lokman@utem.edu.my

Keywords: PID; NPID; tracking performance

ABSTRACT – This paper presents the potential of the nonlinear proportional-integral-derivative (NPID) controller in improving the tracking performance for XY Table Ball screw drive system. This NPID controller employs some nonlinear components which is consisting a sign block. A simulation is conducted and the tracking performance of NPID controller is compared with the tracking performance of the proportional-integral-derivative (PID) controller. A Matlab/Simulink is used to simulate both controller with continuous root mean square (CRMS) and display block. The simulation result shows that the NPID controller produces smaller maximum tracking error and smaller RMSE compared to PID controller.

1. INTRODUCTION

XY Table positioning system is widely used in designing some controllers by previous researchers [1]–[4]. In [1], an auto-tuning feed forward compensator (FFC) is used in order to obtain high and consistent performances for mass production machines. A certain manufacturing and assembly tolerances application is included in this machine. In [2], the potential between two friction models for XY AC servo table is discussed. The partition friction model indicates smaller tracking error compared to static Stribeck model. In addition, [3] analyzes three different friction compensation namely friction model based feed forward, inverse model based disturbance observer and combination of both friction compensations. Next, [4] designed a nonlinear proportional-integral-derivative (NPID) controller in order to compensate the nonlinearity of the system. This NPID controller uses a Popov stability criterion to check its stability. The Fast Fourier Transform (FFT) Error results with 1000 rpm, 2000 rpm and 3000 rpm spindle speed indicate that the NPID controller performs better than PID controller.

In addition, a replicate cutting force data in real system is built to inject in the control system of XY table during simulation process [5].

In 2008, [6] presents a modification of PID controller applied on the electromechanical actuator (EMA) system for aerofin control (AFC). This modification represents an error modification of the system. The simulation and experimental results show that this modification of PID controller has a better transient response compared to conventional PID controller and this is due to the gain will increase when the error is small and vice versa. This paper deals with nonlinear proportional-integral-derivative (NPID) controller in order to control the XY Milling Table Ball Screw Driven System. The NPID controller used some nonlinear component using block diagram MATLAB/Simulink. The aim of this paper is to improve the tracking performance of the system. The performance obtained is described in this paper by comparing NPID controller with PID controller through simulation process.

2. METHODOLOGY

In this study, XY Table Ball Screw Driven System as shown in Figure 1 is used in order to obtain a transfer function. In this paper, only x-axis movement of the system is considered and the system identification is conducted. Hence, the transfer function of the XY Table Ball-screw drive system is as follows:

$$\text{Transfer function} = 78020/ (s^2 + 163s + 193.3) \quad (1)$$

Figure 1 Experimental Setup for XY Table Ball-screw Drive System

The NPID controller is designed in order to compress and expand of the error of the system. This controller uses some nonlinear components consisting of sign, absolute and square root of the error based on the previous study [6]. This modified error is designed as a block diagram using MATLAB/Simulink as shown in Figure 2 and also can be formulated as follows:

$$e_c(t) = \text{sign}\,(e(t)).\,(\,|\,e(t)\,|\,)^{1/2} \quad (2)$$

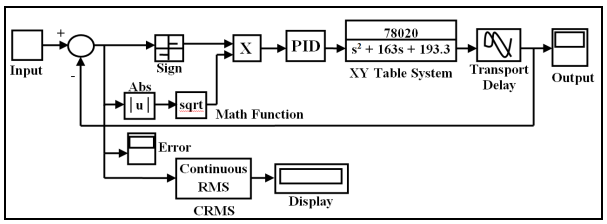

Figure 2 NPID Controller Scheme

3. RESULTS AND DISCUSSION

In this section, simulation validation is performed to evaluate the performance of the NPID and PID controller with sinusoidal input. Furthermore, the amplitude of the system is set to 100 mm. The system is observed for 15 seconds during simulation. In addition, the parameters of PID gains are set to 0.8998, 0.0006077 and 0.005155 for k_p, k_i, k_d, respectively. In order to verify the performance of the NPID controller, two different frequencies are used and set at 0.3 Hz and 0.5 Hz.

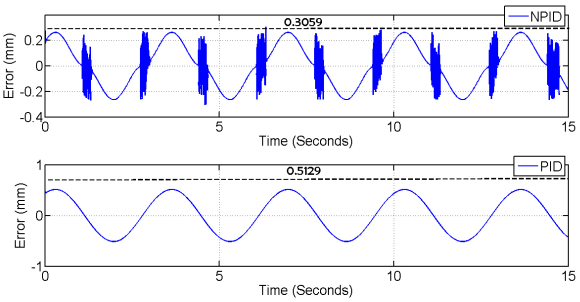

Figure 3 Simulated Maximum Tracking Error at 0.3 Hz

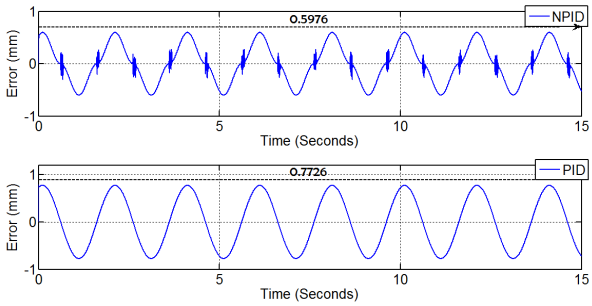

Figure 4 Simulated Maximum Tracking Error at 0.5 Hz

Table 1 Simulated Maximum Tracking Error and RMSE of System with NPID and PID Controller

	0.3 Hz		0.5 Hz	
	PID	NPID	PID	NPID
Maximum Tracking Error (mm)	0.5129	0.3059	0.7726	0.5976
RMSE (mm)	0.3627	0.1680	0.5463	0.3674

In Figure 3, the result indicates that the maximum tracking error for NPID controller is 0.3059 mm while the maximum tracking error for PID controller is 0.5129 mm. Besides, the RMSE for NPID controller is 0.1680 mm while the RMSE for PID controller is 0.3627 mm. On the other hand, in Figure 4, the results show that maximum tracking error for NPID is 0.5976 mm while for PID is 0.7726 mm. After that, the RMSE for NPID is 0.3674 mm while for PID is 0.5463 mm. RMSE is defined as the square root of the average of the square of all errors. The detail simulation results between PID and NPID controller using different frequency is tabulated in Table 1.

4. CONCLUSION

In this paper, the NPID controller is designed in order to control the position of XY Table Ballscrew Drive System. The purpose of the NPID design is to improve the tracking performance. Simulation test is conducted to verify the performance of the NPID controller and found that the maximum tracking error and RMSE is smaller than PID controller.

ACKNOWLEDGMENT

The authors would like to acknowledge the financial support by Universiti Teknikal Malaysia Melaka (UTeM) under FRGS grant with reference number FRGS/1/2016/TK03/FKP-AMC/F00320 and short term grant scheme (PJP) Universiti Teknikal Malaysia Melaka with reference number PJP/2014/FKPPROTOTAIP/S01379.

REFERENCES

[1] Z. Z. Liu, F. L. Luo, and S. M. IEEE, "QFT-Based Robust and Precision Motion Control System for a High Speed Direct-drive XY Table Positioning Mechanism," vol.1, pp. 293–300, 2003.

[2] T. Zhang, C. Lu, and Z. Xi, "Modeling and simulation of nonlinear friction in XY AC servo table," *2006 IEEE Int. Conf. Mechatronics Autom. ICMA 2006*, vol. 2006, pp. 618–622, 2006.

[3] Z. Jamaludin, H. Van Brussel, and J. Swevers, "Friction compensation of an XY feed table using friction-model-based feedforward and an inverse-model-based disturbance observer," *IEEE Trans. Ind. Electron.*, vol. 56, no. 10, pp. 3848–3853, 2009.

[4] L. Abdullah, Z. Jamaludin, J. Jamaludin, M. R. Salleh, B. Abu Bakar, M. N. Maslan, T. . Chiew, and N. a. Rafan, "Design and Analysis of Self-tuned Nonlinear PID Controller for XY Table Ballscrew Drive System," *2nd Int. Symp. Comput. Commun. Control Autom.*, vol. 3, no. 3ca, pp. 419–422, 2013.

[5] L. Abdullah, Z. Jamaludin, and T. Chiew, "Systematic Method for Cutting Forces Characterization for XY Milling Table Ballscrew Drive System," *Int. J.*, no. 6, 2012.

[6] M. R. Ristanovic, D. V Lazic, and I. Indin, "Nonlinear Pid Controller Modification of the Electromechanical Actuator System for Aerofin Control With a Pwm Controlled Dc Motor," *Autom. Control Robot.*, vol. 7, no. Dc, pp. 131–139, 2008.

MWCNTs functionalization and their effects on the mechanical properties of epoxy/MWCNTs nanocomposites

N.A.M. Noor[1], J.A. Razak[1,*], S. Ismail[1], N. Mohamad[1], R. Junid[2]
[1)] Carbon Research Technology Research Group, Advanced Manufacturing Centre, Faculty of Manufacturing Engineering, Universiti Teknikal Malaysia Melaka, Hang Tuah Jaya, 76100, Durian Tunggal, Melaka, Malaysia
[2)] Composite Research Group, Faculty of Mechanical Engineering, Universiti Malaysia Pahang, 26600, Pekan, Pahang, Malaysia

[*]Corresponding e-mail: jeefferie@utem.edu.my

Keywords: MWCNTs functionalization; epoxy based composites; covalent treatment

ABSTRACT – The inert surface characteristic of MWCNTs filler is prompt to agglomeration which limits their usage for many applications. Therefore, MWCNTs surface modification is necessary for a good dispersion and matrix-filler interaction. Amino Propyl Tri-etoxy Silane (APTS) chemical was used to initiate covalent functionalization on MWCNTs surfaces. As a result, the tensile and flexural strength of treated MWCNTs/epoxy composites were increased by 38.69 % and 58.48 %, respectively as compared to the untreated MWCNTs/epoxy composite system. Scanning electron microscopy (SEM) observations shows the improvement in filler dispersion and matrix-filler interaction in after-functionalized MWCNTs based composite samples.

1. INTRODUCTION

Epoxy has been characterized as one of the interesting class of polymer due to its excellent mechanical properties: high strength and stiffness, high chemical, thermal and dimensional stability, as well as, good creep and solvent resistance [1]. However, this thermoset material is brittle and need to be modified. By incorporating epoxy with nano-sized filler, it can toughen the resulted epoxy based products. Among all, carbon nanotubes (CNTs) are the nano-size filler of choice that normally being utilized to further enhance the performance of epoxy based composites.

The challenge met by incorporation of CNTs in composites is the lack of compatibility with hydrophobic polymers. Thus, various chemical modification methods have been explored in order to address this hurdle. According to Ma et al. [2], CNTs has drawback to form a uniform dispersion, which is emerges from strong *van der Waals* interaction between the tubes leading to entanglement in the host matrix. Researchers are still finding ways for manipulation of CNTs within matrix, in tailoring the desired properties of produced composites.

A great challenge in CNTs/polymer composites is to establish a good matrix-filler interface interaction for more efficient stress-transfer, as force is being applied. In this study, we investigate the effect of MWCNTs functionalization to enhance the mechanical properties of epoxy filled MWCNTs nanocomposite through covalent surface treatment approach.

2. METHODOLOGY

2.1 Raw materials and sample preparation

Epoxy system of diglycidylether of bisphenol A (DGEBA) resin cured by amine hardener (Terra Techno Engineering, Malaysia) was used as matrix resin. Amino-propyl tri-etoxy silane (APTS) was used as surfactant for covalent treatment of MWCNTs within an ethanol (C_2H_6O) medium. The MWCNTs filler of grade Flo Tub 9000 Series were purchased from CNano Technology Limited, China and were used as is. For MWCNTs functionalization, ethanol-distilled water at a ratio of 75:25 was prepared with addition of 3 wt. % of APTS. The sonication coupled with stirring action was performed at 80°C within 24 hrs to produce the *f*-MWCNTs filler. FTIR analysis was conducted to confirm the functionalization success.

There were six variations of epoxy/MWCNTs composites were prepared with varied percentages of MWCNTs addition (0, 0.25, 0.50, 0.75, 1.00 and 3.00 wt. %). A conventional mechanical mixing and stirring technique was used to fabricate Epoxy/MWCNTs and Epoxy/*f*-MWCNTs composites (at 1000 rpm, 60 mins). The mixture was then transferred to silicon rubber mold and cured for 60 mins at 110 °C in a drying oven. The prepared samples were then cut into specific dimension required for the tensile and flexural tests, in accordance with the standard methods of ASTM D3039, and ASTM D790, respectively. The SEM observation was performed to observe the morphological tensile fractured surfaces at 300x of magnification.

3. RESULTS AND DISCUSSIONS

3.1 FTIR Analysis of MWCNTs Functionalization

Figure 1 shows a FTIR spectrum for *f*-MWCNTs and untreated MWCNTs. The spectra for *f*-MWCNTs are more stable and uniform than untreated MWCNTs. The chemical functional groups of COOH and COO- that were detected on *f*-MWCNTs actively took part in the polymeric reaction and able to permit functionalization linkages between the MWCNTs and the hosted epoxy matrix. The presence of the new peak and the intensity changes at *f*-MWCNTs spectra shows that the covalent treatment was successfully performed to the MWCNTs surfaces.

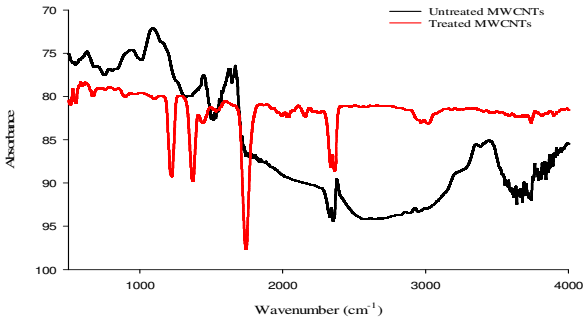

Figure 1 FTIR spectra of treated and untreated MWCNTs

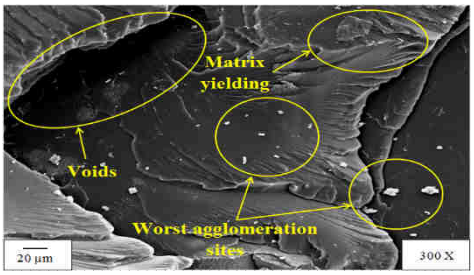

Figure 2 SEM image of fractured surfaces of the epoxy/3.00 wt. % untreated MWCNTs composite at 300x magnification

3.2 Mechanical Properties Evaluation

The tensile performance of *f*-MWCNTs/epoxy composites was compared with untreated MWCNTs/epoxy composites, as depicted in Figure 3. It is noticed that the addition of 0.50 wt. % *f*-MWCNTs provided the highest tensile performance, which is 36.957 MPa with 38.69 % improvement compared to unfilled system. Lower performances of untreated MWCNTs/epoxy system are owed to the agglomeration of filler, over filler-filler interaction and the presence of voids [3] as depicted in Figure 2 of SEM observation.

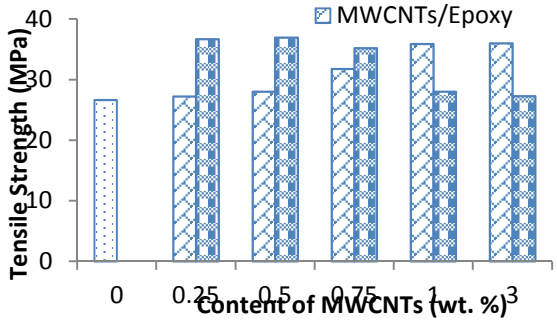

Figure 3 The effect of MWCNTs functionalization towards tensile strength of epoxy/MWCNTs composites

The flexural strength results are depicted as in Figure 4. It shows that the addition of 0.50 wt. % of *f*-MWCNTs had given the highest flexural strength of 79.69 MPa with about 58.48% of improvement. After been functionalized, the functional groups that were attached to the surface of MWCNTs reacted with the matrix during the curing process and later built the covalent linkages. This leads to higher stiffness of composites and gives a drastic increase in the flexural strength performance [4]. An improvement in interfacial bonding between the matrix-filler was enabled an effective stress transfer, leading to a better flexural strength [5].

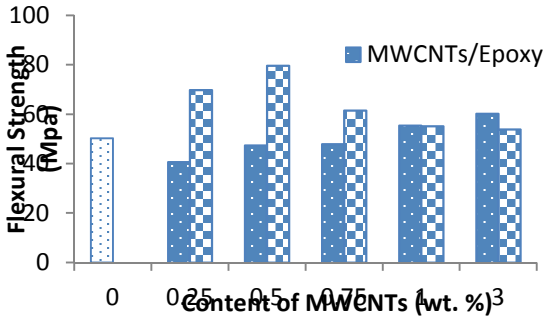

Figure 4 Effect of MWCNTs functionalization toward flexural strength of epoxy/MWCNTs composites

4. CONCLUSIONS

In this study, the surface modification of MWCNTs by covalent approach was successfully performed and confirmed by FTIR spectra results. The addition of 0.50 wt. % of treated MWCNTs had yielded a significant improvement by 38.69% and 58.48% in the tensile strength and flexural strength, respectively. This indicates the success of *f*-MWCNTs covalent surface treatment in improving the matrix-filler interaction that benefits further the resulted properties of epoxy/MWCNTs composites.

ACKNOWLEDGEMENT

We greatly acknowledged the research funding from Research Acculturation Grants Scheme coded RAGS/1/2014/TK04/FKP/B00072 from the Ministry of Higher Education, Malaysia.

REFERENCES

[1] W. Zou, Z. Du, Y. Liu, X. Yang, H. Li, and C. Zhang, "Functionalization of MWNTs using polyacryloyl chloride and the properties of CNT–epoxy matrix nanocomposites," *Compos. Sci. Technol.*, vol. 68, no. 15–16, pp. 3259–3264, 2008.

[2] C. Ma, W. Zhang, Y. Zhu, L. Ji, R. Zhang, N. Koratkar, and J. Liang, "Alignment and dispersion of functionalized carbon nanotubes in polymer composites induced by an electric field," *Carbon N. Y.*, vol. 46, no. 4, pp. 706–710, 2008.

[3] M. M. Rahman, S. Zainuddin, M. V. Hosur, J. E. Malone, M. B. A. Salam, A. Kumar, and S. Jeelani, "Improvements in mechanical and thermo-mechanical properties of e-glass/epoxy composites using amino functionalized MWCNTs," *Compos. Struct.*, vol. 94, no. 8, pp. 2397–2406, 2012.

[4] N. G. Sahoo, S. Rana, J. W. Cho, L. Li, and S. H. Chan, "Polymer nanocomposites based on functionalized carbon nanotubes," *Prog. Polym. Sci.*, vol. 35, no. 7, pp. 837–867, 2010.

[5] M. T. Kim, K. Y. Rhee, S. J. Park, and D. Hui, "Effects of silane-modified carbon nanotubes on flexural and fracture behaviors of carbon nanotube-modified epoxy/basalt composites," *Compos. Part B Eng.*, vol. 43 no. 5, pp. 2298–2302, 2012.

Study on failure index variation of hybrid composite using finite element modelling method

A.F. Ab Ghani[1]*, S. Dharmalingam[1], N.A.A. Md Zahir[1], J. Mahmud[2]

[1)] Faculty of Mechanical Engineering, Universiti Teknikal Malaysia Melaka (UTeM), Melaka, Malaysia
[2)] Faculty of Mechanical Engineering, Universiti Teknologi MARA (UiTM) Shah Alam, Selangor, Malaysia

*Corresponding e-mail: ahmadfuad@utem.edu.my

Keywords: Maximum Stress, Maximum Strain, Composite Failure

ABSTRACT – Last Ply Failure (LPF) failure theory is studied to find out maximum load in occasion when all plies in composite laminas surpassed their maximum stress/strain. It is a method to estimate the maximum load that composite specimen can withstand before whole composite plies/laminate experiences fail/breakage. The study focuses on prediction based on the Maximum Stress Theory and Maximum Strain Theory. The simulation is performed by utilizing software *Ansys* and built in failure theory in the finite element software which is Max Stress and Max Strain. The composite plies comprises of two cases of hybrid composite which formed by Glass Fiber Reinforced Polymer (GFRP) and Carbon Fiber Reinforced Polymer (CFRP).

1. INTRODUCTION

Maximum loads of the composite under tensile loading before it reaches failure due to maximum stress or strain can be assessed using experimental or advance software methods such as finite element modelling. Physical test method is also known as destructive methods. This experimental method required a large number of testing specimen to carry out the test. Hence, the cost require for the experimental methods is very high. Whereas finite element analysis (FEA) is a lower cost tool as compared to experimental method due to do not require a lot of testing specimen and also have the advantage for carry out repeating improving process especially for failure analysis investigation. The failure investigation in this research will focus on last ply failure of laminates where total ruptured when the last ply fails is expected from tensile loading simulation. This is different with First Ply Failure (FPF) which indicates failure initiation also known as initial failure. FEA enable the assessment of stress and strain contour of composite and failure prediction tool [1,2].

2. FAILURE THEORY

The failure prediction is used to predict the progress failure analysis of a structural such as composite material by using failure criteria. Several researchers studied the failure criteria for the limit theories which are maximum stress theories as well as maximum strain criteria. Most of researchers and *Ansys* Manual Documentation suggested that stress component at the material point is considered at failure initiation when ratio greater than or equal to 1 as shown in Equation 1 and Equation 2 [1,2,3,] suggest.

For tensile:

If $\sigma_{11} > 0$, set $X = X_t$; If $\sigma_{22} > 0$, set $Y = Y_t$ (1)

$$\sigma_{11} \geq X_t; \sigma_{22} \geq Y_t; \sigma_{12} \geq S \quad (2)$$

Where σ_{11}, Normal stress in fiber direction, σ_{22}, Normal stress in transverse direction, σ_{12}, Shear stress, X_t, Ultimate tensile strength in fiber direction, Y_t, Ultimate tensile strength in transverse direction and S, Ultimate shear strength. The maximum strain theory is also simple failure measure that used to determine whether the lamina is fail or not. Several researchers have studied the maximum strain theory failure measure is comparing the component of the finding stress with ultimate strength allowable value of a materials as shown in Equation 3 and Equation 4 [2,4]

If $\varepsilon_{11} > 0$, set $X_\varepsilon = X_{\varepsilon_t}$; If $\varepsilon_{22} > 0$, set $Y_\varepsilon = Y_{\varepsilon_t}$ (3)

$$\varepsilon_{11} \geq X_\varepsilon; \varepsilon_{22} \geq Y_\varepsilon; \gamma_{12} \geq S_\varepsilon \quad (4)$$

Where ε_{11}, Normal strain in fiber direction, ε_{22}, Normal strain in transverse direction, γ_{12}, Shear strain, X_{ε_t}, Ultimate tensile strain in fiber direction, Y_{ε_t}, Ultimate tensile strain in transverse direction and S_ε, Ultimate shear strain[2,3].

3. METHODOLOGY

A simulation of tensile test for hybrid composite is performed as accordance to ASTM D3039 operating procedure of 2mm/min. Two sample of hybrid composite are tested and labelled as Hybrid A and Hybrid B. After complete the tensile test will proceed with the failure prediction which is last ply failure. A last ply failure analysis is studied base on maximum stress theory and maximum strain theory. Both Hybrid A and Hybrid B are modelled in two types of elements namely conventional shell and continuum shell. The differences between both elements in finite element modelling are shown in Table 1.

Table 1 Attributes of Conventional/Continuum Shell [5]

	Conventional shell	Continuum shell
Base	Reference surface and 2D geometry	Full 3D geometry
Shape	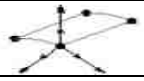	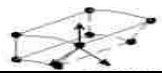
Thickness element	Defined as a sectional property	Defined as nodal geometry
Limitation	When there are large offsets from the shell mid	Can be used for thin or thick shells with more accuracy through

	surface it requires multi constraint	thickness response for composite laminate

4. RESULTS AND DISCUSSION

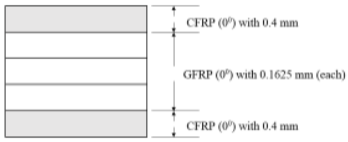

Figure 1 Hybrid A Composite Layup

Table 2 Max Stress and Max Strain Theory using Continuum Shell for Hybrid Composite A

Maximum stress theory

Failure index for each ply and total reaction force for LPF in case 1

Value of failure index for ply		Value of failure index for ply	
Ply 1	1.2260	Ply 3	1.0047
Ply 2	1.0047	Ply 4	1.0047
Ply 5	1.2260		
Total reaction force for LPF	38.76 kN		

Maximum strain theory

Failure index for each ply and total reaction force for LPF in case 1

Value of failure index for ply		Value of failure index for ply	
Ply 1	1.0056	Ply 3	1.0629
Ply 2	1.0629	Ply 4	1.0629
Ply 5	1.0056		
Total reaction force for LPF	29.84 kN		

For continuum shell elements, maximum stress criteria recorded higher reaction force/load as compared to maximum strain criteria as seen in Table 2. Continuum shell is a solid model which will consider the response through the cross section thickness when compare to a flat plan surface of conventional shell with zero thickness. For cases Hybrid A and Hybrid B maximum strain criteria seems underestimate failure load as in Figure 2a and Figure 2b.

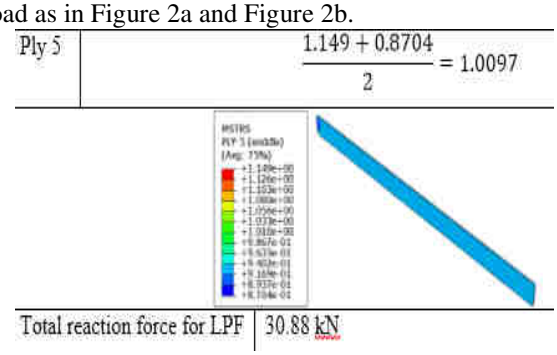

Figure 2a Index Failure for Maximum Stress Hybrid A

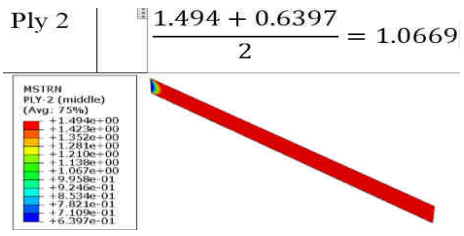

Figure 2b Index Failure Maximum Strain for Hybrid B

Hybrid B as shown in Figure 3 has more carbon plies in the arrangement of the composite, all plies arranged in 0 angle of orientation. Hence, Hybrid B requires more loads to achieve the last ply failure at same level of failure index when compared to Hybrid A as shown in Table 3.

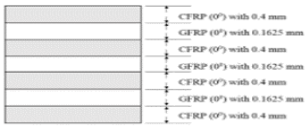

Figure 3 Hybrid B Composite Layup

Table 3 Max Stress and Max Strain Theory using Conventional Shell Elements for Hybrid Composite B

Maximum stress theory

Failure index for each ply and total reaction force for LPF in case 2

Value of failure index for ply		Value of failure index for ply	
Ply 1	1.222	Ply 4	1.0072
Ply 2	1.0072	Ply 5	1.222
Ply 3	1.222	Ply 6	1.0072
Ply 7	1.222		
Total reaction force for LPF	71.31 kN		

Maximum strain theory

Failure index for each ply and total reaction force for LPF in case 2

Value of failure index for ply		Value of failure index for ply	
Ply 1	1.0024	Ply 4	1.0669
Ply 2	1.0669	Ply 5	1.0024
Ply 3	1.0024	Ply 6	1.0669
Ply 7	1.0024		
Total reaction force for LPF	54.90 kN		

Results obtained from the model of continuum shell are more accurate as compared to conventional shell due to the fact that continuum shell elements produce better than conventional shell elements in modelling the transverse shear stress through the thickness [1,4,5].

5. CONCLUSIONS

LPF is a type failure prediction that can be used to estimate the maximum load on composite that can withstand when all plies of the coupon fail completely through tensile test. This failure is predicted by using *Ansys* software with built in failure theory which is maximum stress and maximum strain criteria. The total reaction force of the composite can be affected by layup arrangement and nature of hybrid composition as shown in results.

ACKNOWLEDGEMENT

This research is funded by MOHE via RAGS/1/2015/TK0/UTEM/03/17.

REFERENCES

[1] Matthews & Davies & Hitchings & Soutis, *Finite Element Modelling of Composite Materials and Structures*, 1st Edition, Woodhead Publishing; 2000,

[2] Farooq, U. and Myler, P., "Ply level failure prediction of carbon fibre reinforced laminated composite panels subjected to low velocity drop-weight impact using adaptive meshing techniques", *Acta Astronautica*, Vol 102, pp 169-177, 2014

[3] Reddy, J. and Reddy, J, *Mechanics of laminated composite plates and shells*, Boca Raton: CRC Press.; 2004.

[4] Bakshi, K. and Chakravorty, D., "First ply failure study of thin composite conoidal shells subjected to uniformly distributed load", *Thin-Walled Structures*, 76, 1-7, 2014.

[5] Naceur, H., Shiri, S., Coutellier, D., and Batoz, J., "On the modeling and design of composite multilayered structures using solid-shell finite element model", *Finite Elements In Analysis And Design*, Vol 70-71, pp 1-14, 2013.

Energy absorption analysis of different cross section bumper beam using finite element analysis

S.M. Nasiruddin*, A. Hambali, J. Rosidah

Faculty of Manufacturing Engineering, UniversitiTeknikal Malaysia Melaka,HangTuah Jaya, 76100 Durian Tunggal, Melaka, Malaysia

*Corresponding e-mail: nasirmuhd.91@gmail.com

Keywords: Bumper Beam; Energy Absorption; FEA

ABSTRACT –Bumper beam is a frontal component of a car bumper system which functions is to absorb kinetic energy during crash. The objective of this paper is to study the impact analysis through the different type of cross sections of bumper beam at the conceptual design stage. Five (5) concept designs have been proposed with the different types of cross section and were analysed using ANSYS LS DYNA. The best concept design of bumper beam was determined based on specific energy absorption which was obtained through FEA. Concept design 4 (C4) was selected as the best concept design as it has the highest specific energy absorption compared to other concept designs of the bumper beam.

1. INTRODUCTION

The function of the bumper system is to protect the car body and passengers during crash. It consists of three main components namely fascia, energy absorber and bumper beam as depicted in Figure 1 [1]. The fascia is considered as a non-structural component due to its function to decrease the aerodynamic drag force. The absorber is designed to dampen a portion of the kinetic energy from a collision. The bumper beam is a key structure that helps to absorb the kinetic energy from a high-impact collision and also to provide bending resistance in a low-impact collision [2]. Bumper beam absorbs the impact collision energy in a controlled manner before the energy gets transferred to the passenger compartment.

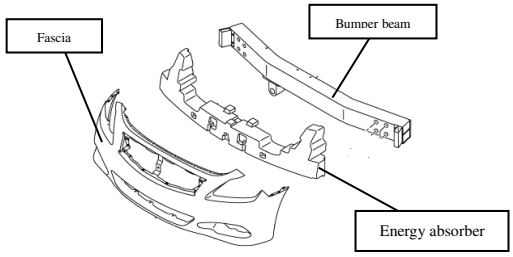

Figure 1 Common bumper system [1]

Increasing the safety for passengers is important as nowadays, automobiles are used extensively and may involve in an accident on the road. Structural crashworthiness is an essential requirement in the design of automobiles. Crashworthiness refers to the response of a vehicle when it is involve in or undergoes an impact. Bumper beam play an important role in automobile crash as it is the key structure that helps absorbing the impact energy. There are many different cross section designs available with different energy absorption capability depend on the type of automobile and its weight. A good crashworthiness performance is when it effect less damaged to the vehicle and passengers after crash. The objective of this paper is to study the energy absorption through the different cross section design of bumper beam.

2. LITERATURE REVIEW

2.1 *Finite Element Analysis*

Analyzing the energy absorption in real impact is quite complicated and depends on different parameters. Finite Element Analysis (FEA) is a suitable method to analyze the energy absorption and determine the approximate impact behavior deflection during an impact. Currently there are many software can be employed to simulate the impact such as ANSYS LS DYNA, LS DYNA, PAMCRASH and ABAQUS. Hambali et al. [3] analyzed the energy absorption of the bumper beam using ANSYS LS DYNA. Low carbon steel was replaced by SMC composite material. Small deflection occurs during simulation, but the result obtained is reasonable as it was within Economic Commission for Europe (ECE) United Nations standard requirement where the parts still intact and usable after the impact. Zhang et al. [4] studied the foam-filled thin-walled composite structures to be an ideal energy absorber for its extraordinary energy absorption ability and lightweight features. The result obtained for overall deformation of the finite element model in terms of collapse mode and number of folds was in good agreement with that of the experiments.

Advantages of Finite Element Analysis are numerous. FEA can analyze the design in detail, saving time and cost by reducing the number of prototypes required for the testing. Because of high cost of physical test and time consuming, FEA analysis is used before conducting the real test performance of impact test where it can speed up an engineering change of an existing product problem or to optimize it. Result obtained by simulation also agrees fairly with the results obtained from experimental [5, 6].

Park et al. [7] developed an optimized bumper beam cross section that satisfies both the safety requirements for a front rigid-wall impact and lower leg injuries in a pedestrian impact test. The study compared the intermediate response surface modeling (IRSM)

with finite element model and maximum displacement error between the two models did not exceed 3%. Kathiresan et al. [8] studied the crashworthiness of glass fibre/epoxy laminated thin walled composite. Results of energy absorption predicted by numerical analysis or finite element analysis results mostly matching with the experimental results.

3. SIMULATION

3.1 *Boundary condition*

The low-speed impact simulation was simulated in ANSYS LS DYNA. The impactor with weight 1000 kg and speed 4 km/h impact at the middle of the bumper beam was considered. The density of material has been changed to follow the ECE regulation where the density of impactor equal to mass of the automobile. Table 1 shows the material properties of sheet moulding compound (SMC). The impactor and car body were modeled as rigid structures with no energy absorption capability.

Table 1 Sheet moulding compound (SMC) properties

Young modulus GPa	Yield strength MPa	Poisson ratio	Density kg/m^3
20	309	0.33	1830

3.2 *New conceptual design bumper beam*

Five concept designs of bumper beam with different cross section have been proposed and its dimension such as height and width are taken based on the existing bumper beam design.

4. RESULTS AND DISCUSSION

A graph of energy versus time was obtained from the FEA. The conservation of energy during the impact process is determined from the curve of the graph. Figure 3 shows the energy versus time graph where kinetic energy is transform into deformation energy. As the kinetic energy keep decreasing during impact the internal energy is increasing. Figure 4 shows the graph of internal energy versus time. It shows the comparison of the energy absorbs by the bumper beam during impact process. Table 2 shows the analysis results of the bumper beam design.

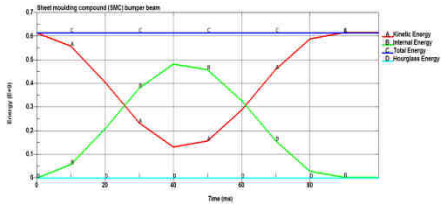

Figure 3 Kinetic energy transfers

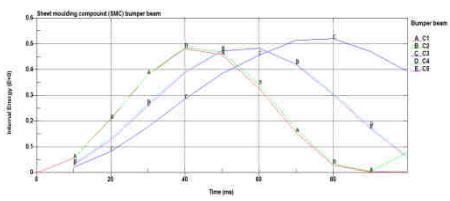

Figure 4 Internal energy

Table 2 Results Summary

Bumper beam design	Cross section	Energy absorption (J)	Weight (kg)	Maximum Deformation (mm)	Specific energy absorption (J/kg)
C1		482.56	0.31753	29.88	1519.73
C2		486.54	0.34488	30.25	1410.75
C3		520.73	0.38147	48.19	1363.15
C4		485.22	0.22562	40.11	2150.61
C5		483.46	0.30289	38.56	1596.16

5. CONCLUSION

Concept design (C4) was the best design due to it has highest value of SEA when impacting structure and absorbs maximum energy during impact with minimum mass.

ACKNOWLEDGEMENT

The authors gratefully acknowledge to Universiti Teknikal Malaysia Melaka (UTeM) for supported this project under FRGS/2/2013/TK04/FKP/02/F00179.

REFERENCES

[1] S. M. Sapuan, M. A. Maleque, M. Hameedullah, M.N. Suddin, and N. Ismail, "A note on the conceptual design of polymeric composite automotive bumper system" *Journal of Materials Processing Technology*. Vol 159, no. 2, pp. 145–151, 2005.

[2] M. M. Davoodi, S. M. Sapuan, , and R. Yunus, "Conceptual Design of a Polymer Composite Automotive Bumper Energy Absorber" *Material and Design*. Vol 29, no. 7, pp. 1447–1452, 2008.

[3] A. Hambali, A. Rabiatul, A. Rahim, and Taufik, "Design Optimization of Automotive Bumper Beam Through Energy Absorption Analysis" *International Journal Engineering of Science*.Vol 3, no. 1,pp. 34–39, 2012.

[4] Y. Zhang, M. Lu, G. Sun, G. Li, and Q. Li, "On Functionally Graded Composite Structures for Crashworthiness" *Composite Structures*. Vol 132, pp. 393–405, 2015.

[5] X. An, Y. Gao, J. Fang, G. Sun, and Q. Li, "Crashworthiness Design for Foam-Filled Thin-Walled Structures with Functionally Lateral Graded Thickness Sheets" *Thin-Walled Structures*. Vol 91, pp. 63–71, 2015.

[6] S. Reddy, M. Abbasi, and M. Fard, "Multi-Cornered Thin-Walled Sheet Metal Members for Enhanced Crashworthiness and Occupant Protection" *Thin-Walled Structures*. Vol 94, pp. 56–66, 2015.

[7] D. K. Park, C. D. Jang, S. B. Lee, S. J. Heo, H. J. Yim, and M. S. Kim," Optimizing the Shape of a Bumper Beam Section Considering Pedestrian Protection" *International Journal of Automotive Technology*. Vol 11, pp. 489−494, 2010.

[8] M. Kathiresan, K. Manisekar, and V. Manikandan, "Crashworthiness Analysis of Glass Fibre/Epoxy Laminated Thin Walled Composite Conical Frusta Under Axial Compression" *Composite Structures*, vol. 108, pp. 584–599, 2014.

Structural and optical properties of nickel sulphoselenide (NiSSe) thin film for photoelectrochemical applications

N. Hazliza, S. Shariza, M. Zaidan, R.K.M Rajes, T. J. S. Anand*

Faculty of Manufacturing Engineering, Universiti Teknikal Malaysia Melaka, Hang Tuah Jaya, 76100 Durian Tunggal, Melaka, Malaysia

*Corresponding e-mail: anand@utem.edu.my

Keywords: Thin film; Electrodeposition; Nickel sulphoselenide

ABSTRACT – NiSSe thin film is being synthesis onto indium tin oxide (ITO) glass substrates using electrodeposition technique and the structural and optical properties of the films are studied. The resulted thin films are characterized using X-ray diffraction analysis and scanning electron microscope to determine the crystallographic and morphological properties. Results proved that nickel sulphoselenide thin films are polycrystalline in nature with a good uniformity. Optical analysis proved the direct bandgap of the films. Well-adherent and dark-coloured thin films are derived from the cathodic electrodeposition. Experimental results proved NiSSe thin films are capable to be used in photoelectrochemical cell application.

1. INTRODUCTION

Usable electric current can be synthesized from photoelectrochemical cells. The unit cells are group together to form a series of solar panel. The arrays of solar panel are generally placed under glass, polymer or plastic as a protection from the weather [1]. The usage of transition metal chalcogenide thin film in solar energy conversion can lead to a good path in developing a bright future for photovoltaic application.

Transition metal chalcogenide are materials of semiconductors, which are capable to be used as an efficient photovoltaic material [2-4]. From the previous research, transition metal chalcogenides NiX_2 (X= Se, S and Te) and MoX_2 (X=Se, S and Te) have been showing a good result in term of optical and semiconducting properties as a new thin film material for solar energy in effort to replace the conventional method [5-9]. Transition metal chalcogenide thin films preparation by electrochemical methods is attracting to be given a special attention as it is relatively affordable, simple and convenient for large area deposition [5].

2. METHODOLOGY

ITO conductive glass substrates are ultrasonically cleaned in ethanol and subsequently in distilled water for 10 minutes each at 60°C [10,11] then dried. The electrolyte use to deposit the NiSSe thin film is derived from aqueous solution of 0.05M nickel (II) sulfate hexahydrate ($NiSO_4.6H_2O$), 0.05M selenium dioxide (SeO_2) and 0.05M sodium thiosulfate pentahydrate ($Na_2S_2O_3.5H_2O$) diluted in 100 ml distilled water. Each material supplies the required Ni^{2+}, Se^{2-} and S^- respectively. 0.03M of additive triethanolamine (TEA) is added into the solution for improving the longevity of the deposition electrolyte as well as the adhesion of the deposited films.

2.1 Cyclic Voltammetry (CV), Electrochemical Deposition and Characterization Techniques.

The range of potential limit between -2.00 to 2.00V for cyclic voltammetry (CV) is selected to determine the suitable potential rate for the electrodeposition to take place by using Princeton Applied Research Model VersaSTAT 3 Potentiostat.

Thin film thickness was measured using gravimetric weight difference method. X-ray diffractograms of the thin film is obtained from a PAN analytical XPERT PROMPD PW 3040/60 diffractometer using monochromatic CuK_α radiation (λ = 1.5148 Å). The morphological analysis of NiSSe thin film was studied by using TM3030 Plus Tabletop Scanning Electron Microscope (SEM) while compositional study was conducted using Swift EDTM3030 Plus Energy Dispersive X-ray Spectroscopy (EDX). Optical absorption are studied using Shimadzu 1700 UV-Vis Spectrophotometer in the wavelength region of 200-1100 nm.

3. RESULTS AND DISCUSSION

Figure 1 shows the cyclic voltammetry of NiSSe where the forward scan begins to rise at higher potential, -1.0 V. During the reverse scan, co-deposition occurs in the negative potential range, however the current value is reduced as the deposition potential is scanned towards more negative value (anodic region). Deposition potentials of -0.9 V is chosen to deposit the NiSSe thin film.

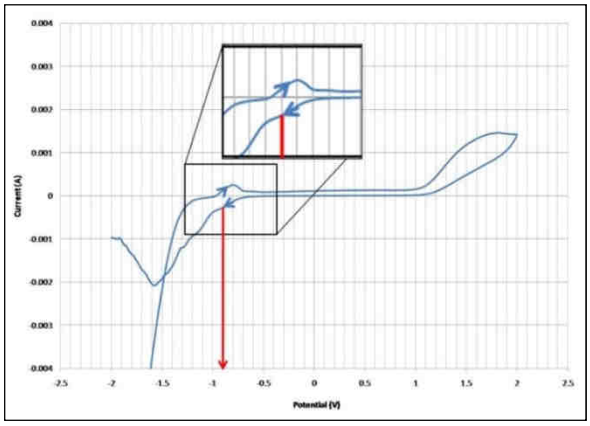

Figure 1 Cyclic voltammogram of NiSSe electrolyte

The structural characterization and analysis using XRD are performed by set the incidence angle 1.5° in order to reduce the intensity of the radiation reflected by the substrate.

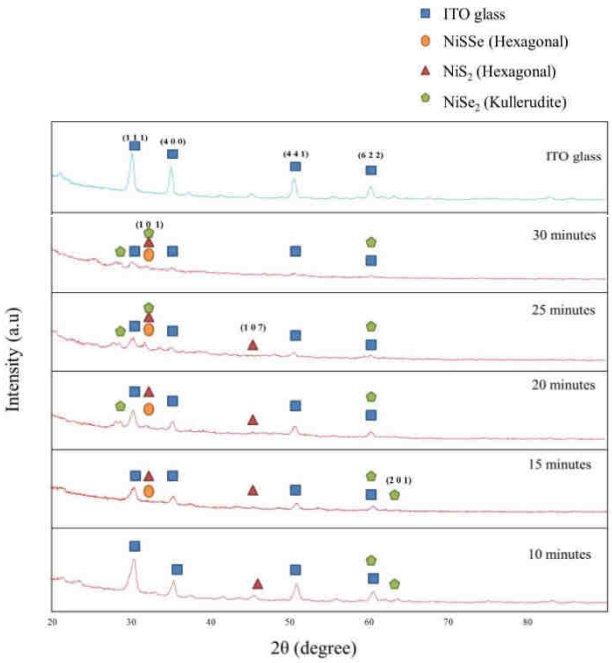

Figure 2 X-ray diffraction pattern of NiSSe thin films deposited at various deposition time

The surface morphology of NiSSe thin films are shown in Figure 3 deposited with different deposition time. It is recognized that the unsymmetrical crystallites forms on ternary chalcogenide films as observed in NiSSe thin film due to the separation of chalcogenides phases (selenium and sulphide) [9].

The positive slope of the plot of $(\alpha hv)^2$ with respect to photon energy show that the thin film of NiSSe have the properties of direct bandgap. The band gap values obtain from the extrapolation of the plot of $(\alpha hv)^2$ with respect to photon energy, E_g for NiSSe thin film. The energy band gap increase from 0.1 eV to 0.8 eV as the deposition time increase and after 25 minutes, the energy band gap decrease to 0.7 eV.

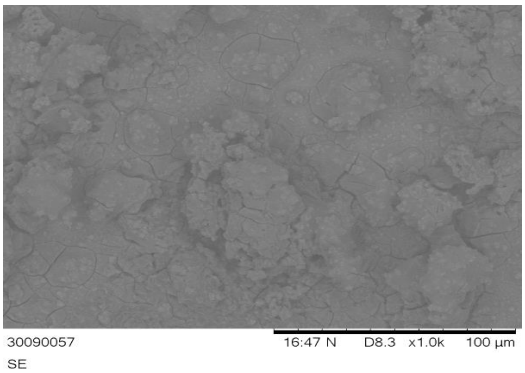

Figure 3 SEM planar images of NiSSe thin film deposited at 30 minutes deposition time under 1000x magnification

4. CONCLUSIONS

To be concluded, NiSSe thin films are successfully deposited on ITO-coated glass. All films obtained are well adhered to the substrates undergoing 'ion-by-ion' growth mechanism. XRD analysis of the films proved that NiSSe thin films are polycrystalline in nature. The morphological characteristics show that the NiSSe are well distributed onto the ITO glass substrates. Optical studies show the direct optical band gap energy of the film. Semiconductor parameters of the film revealed that the NiSSe thin films are p-type material showing that thin films are capable as photoelectrochemical cell material.

ACKNOWLEDGEMENT

The work presented in this paper was supported by Universiti Teknikal Malaysia Melaka (UTeM) and MoHE sponsored FRGS (FRGS/2011/FKP/ TK02/1/F00120).

REFERENCES

[1] Dhanasekaran,V., Mahalingam, T., Rhee and J.K., Chiu, "Structural and optical properties of electrosynthesized ZnSe thin films," *Optik*, vol. 124(3), pp. 255, 2013.

[2] Yadav A.A. and Masumdar E.U. "Photoelectrochemical performances, of n-$CdS_{1-x}Se_x$ thin films prepared by spray pyrolysis technique," *Solar Energy*, vol. 84, pp. 1445, 2010.

[3] Gujarathi D.N, Solanki G.K, Deshpande M.P, and Agarwal M.K., "PEC behaviour of mixed single crystals of tungsten sulphoselenide grown by a CVT technique," *Solar Energy Materials and Solar Cells*, vol. 90, pp. 2630, 2006.

[4] Kokate A.V, Asabe M.R, Delekar S.D, Gavali L.V, Mulla L.S, Hankare P.P, and Chougule B.K., "Photoelectrochemical properties of electrochemically deposited $CdIn_2S_4$ thin films," *Journal of Physics and Chemistry of Solids*, vol. 67, pp. 2331, 2006.

[5] Pathan, H.M. and Lokhande, C.D., "Deposition of metal chalcogenide thin films by successive ionic layer adsorption and reaction (SILAR) method," *Bulletin Material Science*, vol. 27(2), pp.85, 2004.

[6] Anand T.J.S., Zaidan M.A.A., and Shariza S, "Effect of additives on optical measurements of $NiSe_2$ thin films," *Procedia Engineering*, vol. 53, pp. 555, 2013a.

[7] Anand, T.J.S., Rajes K.M., and Mohd Zaidan A.A. "Electrosynthesized NiS_2 thin film and their optical and semiconductor studies," *Reports in Electrochemistry*, vol. 3, pp. 25, 2013b.

[8] Shariza, S. and Anand, T.J.S., "Effect of Deposition Time on Structural and Optical Properties of Molybdenum Chalcogenides Thin Films," *Chalcogenide Letters*, vol. 8(9), pp. 529, 2011.

[9] Anand, T.J.S., and Shariza S., "A study on molybdenum sulphoselenide (MoS_xSe_{2-x}, $0 < x < 2$) thin films: growth from solution and its properties," *Electrochimica Acta*, vol. 81, pp. 64, 2012.